

Article

Primary Evaluation of the GCOM-C Aerosol Products at 380 nm Using Ground-Based Sky Radiometer Observations

Hossain Mohammed Syedul Hoque^{1,*} , Hitoshi Irie², Alessandro Damiani² and Masahiro Momoi² 

¹ Graduate School of Environmental Studies, Nagoya University, Furocho, Chikusa Ward, Aichi 464-8601, Japan

² Center for Environmental Remote Sensing (CEReS), Chiba University, 1-33, Yayoicho, Inage Ward, Chiba 263-8522, Japan; hitoshi.irie@chiba-u.jp (H.I.); damiani@chiba-u.jp (A.D.); m-momoi@chiba-u.jp (M.M.)

* Correspondence: hoque.hossain.mohammed.syedul@a.mbox.nagoya-u.ac.jp or hoquesyedul@gmail.com

Received: 16 July 2020; Accepted: 16 August 2020; Published: 18 August 2020



Abstract: The Global Change Observation Mission-Climate (GCOM-C) is currently the only satellite sensor providing aerosol optical thickness (AOT) in the ultraviolet (UV) region during the morning overpass time. The observations in the UV region are important to detect the presence of absorbing aerosols in the atmosphere. The recently available GCOM-C dataset of AOT at 380 nm for January to September 2019 were evaluated using ground-based SKYNET sky radiometer measurements at Chiba, Japan (35.62° N, 140.10° E) and Phimai, central Thailand (15.18° N, 102.56° E), representing urban and rural sites, respectively. AOT retrieved from sky radiometer observations in Chiba and Phimai was compared with coincident AERONET and multi-axis differential optical absorption spectroscopy (MAX-DOAS) AOT values, respectively. Under clear sky conditions, the datasets showed good agreement. The sky radiometer and GCOM-C AOT values showed a positive correlation (R) of ~ 0.73 for both sites, and agreement between the datasets was mostly within ± 0.2 (the number of coincident points at both sites was less than 50 for the coincidence criterion of ≤ 30 km). At Chiba, greater differences in the AOT values were primarily related to cloud screening in the datasets. The mean bias error (MBE) (GCOM-C – sky radiometer) for the Chiba site was -0.02 for a coincidence criterion of ≤ 10 km. For a similar coincidence criterion, the MBE values were higher for observations at the Phimai site. This difference was potentially related to the strong influence of biomass burning during the dry season (Jan–Apr). The diurnal variations in AOT, inferred from the combination of GCOM-C and ozone monitoring instrument (OMI) observations, showed good agreement with the sky radiometer data, despite the differences in the absolute AOT values. Over Phimai, the AOT diurnal variations from the satellite and sky radiometer observations were different, likely due to the large differences in the AOT values during the dry season.

Keywords: GCOM-C; sky radiometer; aerosol optical thickness (AOT)

1. Introduction

Atmospheric aerosols play a crucial role in controlling Earth's radiation budget and thus impact regional climates and hydrological cycles. High near-surface concentrations of aerosol particles impact air quality and human health [1,2]. Global characterization of aerosols (and their effects on the climate) is difficult due to large spatial and temporal variability in their abundance and properties [3]. Satellite observations of aerosols are useful for understanding the large variability of aerosols in space and time [4–6]. Since 1990, a variety of sensors have been launched on Terra, Aqua, Aura, CALIPSO,

and other satellites [7,8]. In general, large uncertainties occur in satellite aerosol products due to approximations and assumptions in the retrieval process [2]. For example, the combined analysis of aerosol robotic network (AERONET) and ozone monitoring instrument (OMI) aerosol optical thickness (AOT) at 440 nm has shown that more than 35% of OMI AOT is higher than the expected uncertainty of 30% (AOT ~ 0.1) [9]. Therefore, ground-based observations under the different surface and atmospheric conditions are required to evaluate the uncertainties in satellite aerosol parameters.

One of the important aspects of aerosol retrieval in the ultraviolet (UV) region is the detection of brown carbon (BrC). BrC is the UV light absorbing component of organic aerosols (OA). In most climate models, OA is treated as purely scattering. However, recent laboratory studies [10,11] have shown that BrC can increase net absorption by OA emitted from biomass burning. Thus, the potential climate impact of BrC is currently under discussion. Moreover, aerosol properties retrieved from the UV channel are less affected by uncertainties due to surface reflectivity [12].

OMI is currently the only instrument providing AOT in the UV region during the afternoon overpass time (13:30 Local Time). OMI is the successor of the total ozone mapping spectrometer (TOMS) series with a spatial resolution of $13 \times 24 \text{ km}^2$ at nadir. Various studies have performed the accuracy assessment of the aerosol optical properties retrieved from the OMI UV channel [9,13–15]. Ahn et al. [9] reported a correlation coefficient (R) of 0.75 between coincident AERONET and OMI AOT at 388 nm at more than 22 sites. The OMI aerosol products also show good agreement with collocated moderate resolution imaging spectrometer (MODIS) and Terra/multiangle imaging spectroradiometer (MISR) aerosol products at 500 nm. However, due to subpixel cloud contamination of OMI footprints, the retrieved aerosol products tend to be overestimated [16].

The Global Change Observation Mission-Climate (GCOM-C) satellite was launched by the Japanese Aerospace Exploration Agency on December 23, 2017. Its mission objective is to observe geophysical variables related to the land, atmosphere, ocean, and cryosphere. GCOM-C overpass occurs around 10:30 LT. Aerosol optical properties in the UV to near-infrared (NIR) region are retrieved from the GCOM-C observations. The spatial resolution of 10 km (0.1°) is used for the GCOM-C aerosol retrievals. Thus, GCOM-C is currently the only satellite providing UV aerosol products during the morning overpass time with an improved spatial resolution.

In this study, sky radiometer observations from January–September 2019 at Chiba (Japan) and Phimai (central Thailand) were used to evaluate the GCOM-C AOT data at 380 nm. The ground-based observation period was chosen based on the availability of satellite data. Sky radiometer measurements at Chiba and Phimai were first compared with the coincident AERONET [17] and multi-axis differential optical absorption spectroscopy (MAX-DOAS) observations, respectively. Then, the days of overlap between sky radiometer and GCOM-C observations were evaluated in terms of AOT values at 380 nm. The aerosol composition in Chiba, based on the absorption Angstrom exponent (AAE), extinction Angstrom exponent (EAE), and volume size distribution, was also discussed. The aerosol composition in Phimai was discussed in detail by Irie et al. [18]. The diurnal variations in the AOT at 380 nm inferred from the combination of GCOM-C and OMI observations were also discussed.

2. Ground-Based Observations

We considered ground-based remote sensing observations at the sky radiometer network (SKYNET) Chiba (35.62° N , 140.10° E) and Phimai (15.18° N , 102.56° E) sites. SKYNET is an international ground-based remote sensing network for aerosol and radiation research. Chiba is an urban site located $\sim 40 \text{ km}$ southeast of Tokyo. Phimai is a rural site in central Thailand ($\sim 260 \text{ km}$ northeast of Bangkok). The sky radiometer (POM-02; Prede Co., Ltd, Tokyo, Japan) is a sun-sky photometer that measures direct and diffuse solar irradiance [18]. In addition to sky radiometers, multi-axis differential optical absorption spectroscopy (MAX-DOAS) instruments are installed at both sites. MAX-DOAS measures scattered sunlight at several elevation angles (ELs) between the horizon and the zenith over the wavelength range from UV to visible [19,20]. The two SKYNET stations were selected because they have multi-instrument observation facilities and represent different surface cover types (i.e., urban

and rural). The retrieval of aerosol optical properties from the sky radiometer and MAX-DOAS observations are discussed in Section 3.

3. Datasets and Methods

The datasets used in this study are summarized in Table 1. The datasets are explained in the subsequent sections.

Table 1. The datasets used in the study and the uncertainties in the retrieved product.

Dataset	Uncertainty in the Retrieved Product	Reference
GCOM-C AOT at 380 nm	± 0.15	Yoshida et al. [21]
OMI AOT at 380 nm	± 0.10	Ahn et al. [9]
SKYNET AOT at 380, 500, and 675 nm	± 0.02	Irie et al. [18]
AERONET AOT at 380, 500, and 675 nm	± 0.02	Holben et al. [17]
MAX-DOAS AOT at 476 nm	± 0.05	Irie et al. [20]
MAX-DOAS CHOCHO VCD	20 % (Total error)	Hoque et al. [22]

GCOM-C: Global change observation mission-climate; AOT: Aerosol optical thickness; OMI: Ozone monitoring instrument; SKYNET: Sky radiometer network; AERONET: Aerosol robotic network MAX-DOAS: Multi-axis differential optical absorption spectroscopy; CHOCHO: glyoxal; VCD: Vertical column density.

3.1. Satellite Dataset

3.1.1. GCOM-C Data

GCOM-C carries a multi-spectral optical sensor called the second-generation global imager (SGLI), which is the successor to the Global Imager Onboard Advanced Earth Observing Satellite-II [23]. The SGLI consists of two radiometers, the visible and near-infrared radiometer (VNR) and the infrared scanner (IRS), covering the radiation observations over the wavelength range from near-ultraviolet (UV) to infrared. The SGLI-VNR observes polarized and non-polarized radiance. The VNR uses a wide-swath (1150 km) push-broom scan with a line CCD detector. On the other hand, the IRS uses the conventional cross-track mirror scan system with a 1400 km swath width. SGLI has 19 channels, including two polarization channels in the visible and near-infrared (NIR) regions [24,25]. The specifications of the SGLI channels are given in Table 2. The relative spectral response of the GCOM-C VNIR channels is shown in Figure 1.

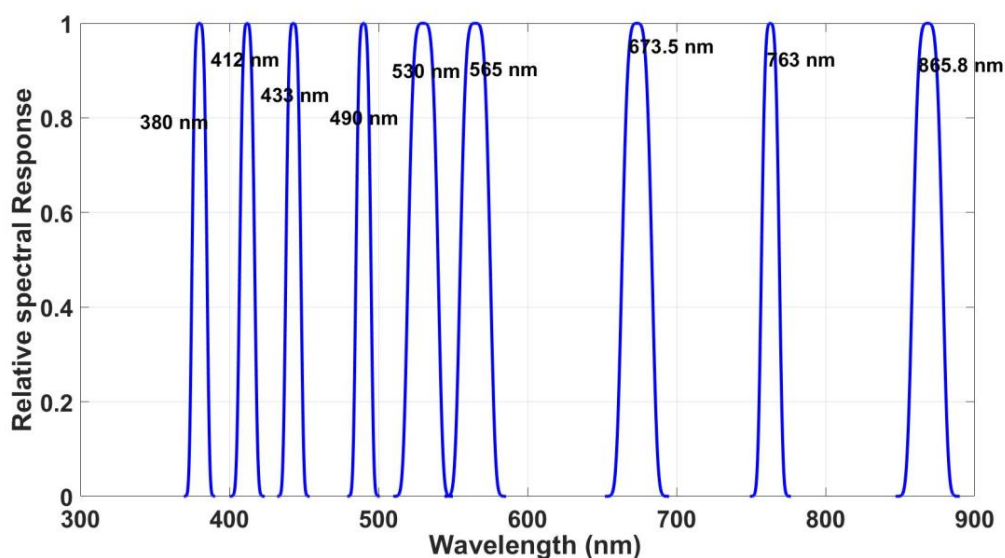


Figure 1. The relative spectral response of the global change observation mission-climate (GCOM-C) visible and near-infrared (VNIR) channels. The spectral response data were obtained from the GCOM-C official portal (https://suzaku.eorc.jaxa.jp/GCOM_C/instruments/files/sgli_rsr_f_for_algorithm_201008.txt).

Table 2. Specifications of the SGLI channels.

Channel	Center Wavelength (nm)	Bandwidth (nm)	L_{std}	SNR	IFOV (m)
VNR1	380	10	60 W/m ² /sr/μm	250	250
VNR2	412	10	75 W/m ² /sr/μm	400	250
VNR3	443	10	64 W/m ² /sr/μm	300	250
VNR4	490	10	53 W/m ² /sr/μm	400	250
VNR5	530	20	41 W/m ² /sr/μm	250	250
VNR6	565	20	33 W/m ² /sr/μm	400	250
VNR7	673	20	23 W/m ² /sr/μm	400	250
VNR8	673	20	25 W/m ² /sr/μm	250	250
VNR9	763	12	40 W/m ² /sr/μm	1200	1000
VNR10	868	20	8 W/m ² /sr/μm	400	250
VNR11	868	20	30 W/m ² /sr/μm	200	250
P1	673	20	25 W/m ² /sr/μm	250	1000
P2	868	20	30 W/m ² /sr/μm	250	1000
SW1	1050	20	57 W/m ² /sr/μm	500	1000
SW2	1380	20	8 W/m ² /sr/μm	150	1000
SW3	1630	200	3 W/m ² /sr/μm	57	250
SW4	2210	50	1.9 W/m ² /sr/μm	211	1000
T1	10,800	740	300 K	0.2	500
T2	12,000	740	300 K	0.2	500

SGLI: Second-generation global imager; **VNR:** Visible and near-infrared channel; **P:** Polarimetry; **SW:** Short wave channel; **T:** Thermal channel; **SNR:** Signal to noise ratio; L_{std} : Standard radiance for SNR; **IFOV:** Instantaneous field of view.

The effectiveness of polarization and UV wavelengths for aerosol data retrieval was demonstrated by the polarization and directionality of Earth's reflectances (POLDER) and total ozone mapping spectrometer (TOMS) instruments, respectively [26,27]. GCOM-C utilizes both the polarization channel and near-UV data to retrieve aerosol information from SGLI observations.

To maintain data observation quality and estimate the instrumental error, the on-orbit and calibration maneuvers are performed periodically. Table 3 shows the type of calibration performed for the SGLI instrument.

Table 3. Types of calibration conducted on the SGLI instrument.

Channel	On-orbit Calibration					Calibration Maneuver		
	Solar Diffuser	Internal Lamp	Dark Image	Black Body	Deep Space	Lunar Calibration	Solar Angle Correction	90-Deg Yaw Maneuver
VNR	1/8 days	1/8 days	1/8 days	None	None	1/month	1/year	1/year
SWIR	1/8 days	1/8 days	1/8 days	None	Per scan	1/month	1/year	None
TIR	None	None	None	Per scan	Per scan	1/month	None	None

SWIR: Short wave infrared channel; TIR: Thermal infrared channel.

A more detailed description of the SGLI instrument and calibration can be found in [23,28,29].

3.1.2. GCOM-C Aerosol Retrieval

GCOM-C AOT data at 380 nm was obtained from the GCOM-C standard data platform (<https://gportal.jaxa.jp/gpr/?lang=en>). GCOM-C has 19 channels, including near-UV (380 nm) and violet (412 nm) wavelengths and polarization channels in the red (670 nm) and NIR (865) regions. All channels from UV to NIR without significant gas absorption are used for retrieval of aerosols over land. Only the channels at wavelengths longer than 800 nm are used for aerosol retrieval over the ocean. Different algorithms are applied to the polarization and non-polarization channels. Only the retrieval of aerosols in the non-polarization channel is discussed here.

(a) Pre-retrieval calculated parameters

At first, simulated top of atmosphere (TOA) radiances are calculated using the radiative transfer model STAR [30–32]. The TOA reflectance at a particular channel i is approximated by the following equation:

$$\rho_i^{sim}(\theta_o, \theta, \varphi) = \rho_i^a(\theta_o, \theta, \varphi) + \frac{t_i^s(\theta_o) * t_i^v(\theta) * \rho_i^s(\theta_o, \theta, \varphi)}{1 - s_i * \rho_i^s(\theta_o, \theta, \varphi)} \quad (1)$$

where ρ_i^{sim} is the TOA reflectance at the channel i , ρ_i^a is the atmospheric path reflectance, t_i^s is the total transmittance from the sun to the surface, t_i^v is the total transmittance from the surface to the sensor, ρ_i^s is the surface reflectance, s_i is the spectral albedo for the illumination of the atmosphere from the ground, θ_o is the solar zenith angle, θ is the satellite zenith angle, and φ is the sun/satellite relative azimuth angle. Secondly, the parameters in Equation (1) are precomputed for each candidate aerosol model. The aerosol models were assumed as an external mixture of the fine and coarse particles. The fine-mode aerosol and dust particle properties were set according to Omar et al. [33], based on global observations of aerosols from the AERONET [17] network. The coarse-mode model settings were based on the study of Sayer et al. [34]. The monomodal lognormal volume size distribution (r_d) used for the aerosol size of the fine and coarse mode models was

$$\frac{dVr_d}{dlnr_d} = \frac{C_v}{\sqrt{2\pi}ln\sigma} \exp\left[-\frac{(lnr_d - lnr_v)^2}{2ln^2\sigma}\right] \quad (2)$$

where C_v is the particle volume concentration, r_v is the volume median radius, and σ is the standard deviation. The $r_v(\sigma)$ values were set to 0.143(1.537), 2.59(2.054), and 2.834(1.908) for fine, coarse marine, and coarse dust, respectively. The aerosol shape was assumed to be spherical in the fine and coarse marine model, whereas the non-spherical shape was assumed in the coarse dust model. The non-spherical parameters of the dust model were calculated based on the work of Nakajima et al. [35]. The real part of the refractive imaginary index for fine, coarse marine, and coarse dust were set to 1.439, 1.362, and 1.452, respectively. The imaginary part of the refractive index (m_i) for coarse marine and dust was set to 3×10^{-9} and 0.0036, respectively, whereas the m_i for the fine mode aerosols was perturbed to account for absorbing and non-absorbing aerosols. The aerosol models are summarized in Table 4.

Table 4. Summary of the aerosol model types used in the GCOM-C retrieval algorithm.

Range of AOT Simulated	Aerosol Type	Reference	Volume Mean Radius
0–2.0	Fine-mode aerosol	Omar et al. [33]	$0.143 \pm 1.58 \mu\text{m}$
	Dust aerosol	Omar et al. [33]	$2.834 \pm 1.90 \mu\text{m}$
	Coarse-mode aerosol	Sayer et al. [34]	$2.59 \pm 2.05 \mu\text{m}$

(b) Retrieval of aerosol optical and physical properties

In the first step of the retrieval, the clear-sky pixel was selected initially using the cloud detection algorithm developed by Ishida et al. [36,37]. Secondly, the precalculated TOA reflectance was corrected for gas absorption, specifically for ozone and water vapor. Total ozone columns from OMI and water vapor columns from the Japan meteorological agency (JMA) global analysis dataset were used. Finally, the optimal estimation method [38] was used to retrieve the aerosol parameter. The outputs of the retrieval algorithm were AOT, Angstrom exponent (AE), single scattering albedo (SSA), and quality assurance (QA) flag. The data were screened based on quality and cloud flags included within the dataset. Only data from clear days (based on the GCOM-C cloud flag) were used for comparison with sky radiometer observations. The product version 1 was used in the current analysis. The details of the non-polarization aerosol product are explained in the work of Yoshida et al. [21]. Moreover, a detailed

description of the retrieval algorithm is provided in the algorithm's theoretical basis document available in the following link https://suzaku.eorc.jaxa.jp/GCOM_C/data/product_std.html.

3.1.3. OMI Aerosol Product

OMI-observed near-UV radiances at 354 and 388 nm and the inversion algorithm named OMAERUV (OMI near UV aerosol retrieval algorithm) were used to derive the aerosol optical depth and single scattering albedo at 388 nm. The Lambertian equivalent reflectivity at 388 nm, the difference between reflectivity at the TOA and surface, and aerosol index were used in the OMAERUV algorithm [8]. The details of the OMI aerosol products have been documented in the work of Torres et al. [39,40], Jethva and Torres [41], and Ahn et al. [16]. The OMI aerosol product at 388 nm used in this study was obtained from the NASA Goddard Earth Sciences and Information services center server (<https://avdc.gsfc.nasa.gov/pub/data/satellite/Aura/OMI/V03/L2OVP/OMAERUV/txt/>) (last browsed on 10 January 2020). The OMI overpass time occurred at 13:30 LT.

3.2. Ground-Based Dataset

3.2.1. Sky Radiometer Observations of Aerosol Optical Properties

SKYNET sky radiometers conducted observations of direct radiance, angular sky radiance, and zenith sky radiance at 11 wavelengths with a temporal resolution of 10 min. The direct and diffuse radiances were measured within 160° of the center of the sun with a field of view of 1° . The AOT, single scattering albedo (SSA), and refractive indexes at 340, 380, 400, 500, 675, 870, and 1020 nm were retrieved using the sky radiometer analysis package, Center for Environmental Remote Sensing (SR-CEReS, version 1) [42]. All pre- and post-processing was conducted using SKYRAD.pack version 5 [43], implemented in SR-CEReS for near-real-time data output. SKYNET sky radiometers used an on-site calibration method, called the improved Langley (IL) method [44], to determine the calibration constant (F_0). The solar disk sextant (SDS) method [44–46] was employed to calculate the solid viewing angle (SVA). The cloud screening algorithm of the sky radiometer data consists of three steps: (1) test with global irradiance data, (2) spectral variability test, and (3) statistical analyses test. The first test detects cloud affected data, and the spectral variability algorithm is applied to detect clear sky data. The final test detects outliers (if any) from clear sky data detected by the previous two steps. The detailed cloud screening algorithm is explained in the work of Khatri and Takamura [47]. The number of clear sky and cloudy data points retrieved from the sky radiometer observations at both sites are summarized in Table 5. Retrievals from SR-CEReS were validated during the NASA KORUS-AQ (Korea-US Air Quality) campaign in 2016 [42].

Table 5. The number of clear sky and cloudy data points for Chiba and Phimai sites retrieved from the sky radiometer observations. The data are shown for the observation period from January 2019 to September 2019.

Site	Clear Sky	Cloudy	Total Retrieved Data Points
Chiba	7072	1604	8676
Phimai	5140	879	6019

3.2.2. MAX-DOAS Observations of Aerosol and Trace Gases

The MAX-DOAS instrument is equipped with an ultraviolet-visible (UV-VIS) spectrometer (Maya2000Pro; Ocean Optics), which is located indoors. A telescope unit consisting of a single fixed telescope and a movable 45° inclined mirror on a rotary actuator is located outdoors and conducts reference and off-axis observations. Scattered sunlight was measured at six ELs of 2° , 3° , 4° , 6° , 8° , and 70° every 15 min. The off-axis ELs were limited to below 10° . This limitation is expected to minimize systematic error in the oxygen collision complex (O_4) fittings while maintaining high measurement sensitivity in the lowest layers of the aerosol and trace gas profiles [20]. High-resolution spectra

were recorded from 310 to 515 nm (full width at half maximum of 0.4 at 386 and 476 nm). Wavelength calibration was performed using a high-resolution solar spectrum from [48]. The measured spectra were analyzed using the Japanese vertical profile retrieval algorithm version 2 (JM2) [20,49]. Aerosol information was retrieved from the O_4 absorption data. JM2 retrieves the vertical aerosol profile in two steps. First, O_4 differential slant column density ($O_4 \Delta SC$) at 357 and 476 nm are retrieved using the DOAS method [50], which is a nonlinear least-squares spectral fitting technique. Significant O_4 absorption values in the wavelength ranges of 338–370 and 460–490 nm were used to determine $O_4 \Delta SC$ values. Second, the aerosol vertical profile is retrieved using $O_4 \Delta SC$ values, and the differential air mass factor is computed (accounting for all ELs). The second retrieval step of JM2 is based on the optimal estimation method [38]. The retrieval procedures and error estimates are explained in detail by Irie et al. [20,49,51,52].

In addition to the aerosol products, glyoxal (CHOCHO) vertical column density (VCD) retrieved from the MAX-DOAS observations were also utilized. VCD and CHOCHO concentration data were retrieved using the JM2 algorithm. The fitting window of 436–490 nm was used for the CHOCHO retrievals. The CHOCHO retrieval procedure is explained in detail by Hoque et al. [22]. MAX-DOAS observations represented a horizontal resolution of ~ 10 km.

To minimize the impact of clouds on the MAX-DOAS retrievals, data screening was performed. First, retrieved AOT greater than 3 (the highest value in the lookup table) was excluded. Such large AOT values potentially occur due to optically thick clouds. Further data screening criterion was based on the fitting residuals of $O_4 \Delta SC$ and the trace ΔSC (glyoxal slant column density (CHOCHO ΔSC) for this study). The screening criterion was—(1) $O_4 \Delta SC$ residuals less than 10%, (2) CHOCHO ΔSC less than 50%, and (3) degree of freedom greater than 1.02. The details of the cloud screening procedure are explained in the work of Irie et al. [20,49].

3.2.3. AERONET Aerosol Data

AERONET is a network of automatic robotic sun and sky-scanning radiometers, which has more than 100 sites around the globe. AERONET data provides quality-assured aerosol optical properties to assess and validate satellite retrievals. The automated sun and sky scanning radiometers (CIMEL) measured direct sunlight with a 1.2° viewing geometry, every 15 minutes at 340, 380, 440, 500, 675, 870, 940, and 1020 nm. It took ~ 8 s to scan all eight wavelengths, with a motor-driven filter wheel positioning each filter in front of the detector. Then, the solar extinction measurements were utilized to retrieve the AOT values at every wavelength except for the 940 nm channel, which is dedicated to perceptible water content retrievals. Multiple algorithm parameters and statistical tests were utilized to minimize cloud impact on AERONET observations. The detailed cloud screening procedures of the AERONET observations are explained by Giles et al. [53]. The details of the AERONET retrievals are explained in the work of [17].

3.3. Methods

3.3.1. Sky Radiometer and AERONET Observations in Chiba

The consistency of the sky radiometer AOT values in Chiba was checked using an independent aerosol dataset from the coincident AERONET observations. AERONET observations were also used as additional information to explain aerosol characteristics in Chiba. Figure 2 shows the comparison between the SKYNET and AERONET (level 1.5, Version 3.0) AOT values at 380, 500, and 675 nm for the observation period from January to December 2019. Only clear sky days (based on the cloud flag in both datasets) were plotted. The statistics of the comparison is given in Table 6. The datasets showed excellent agreement at all three wavelengths, with a correlation coefficient (R) of ~ 0.99 . Thus, the absolute values and temporal variations of AOT values from both sources were quite similar. At all three wavelengths, the datasets generally agreed within ± 0.02 . Greater differences in a few cases could be attributed to differences in the retrieval procedure and cloud influences on both datasets.

Overall, the excellent agreement allowed confidence in the quality of the SR-CEReS retrieval products for evaluating GCOM-C observations.

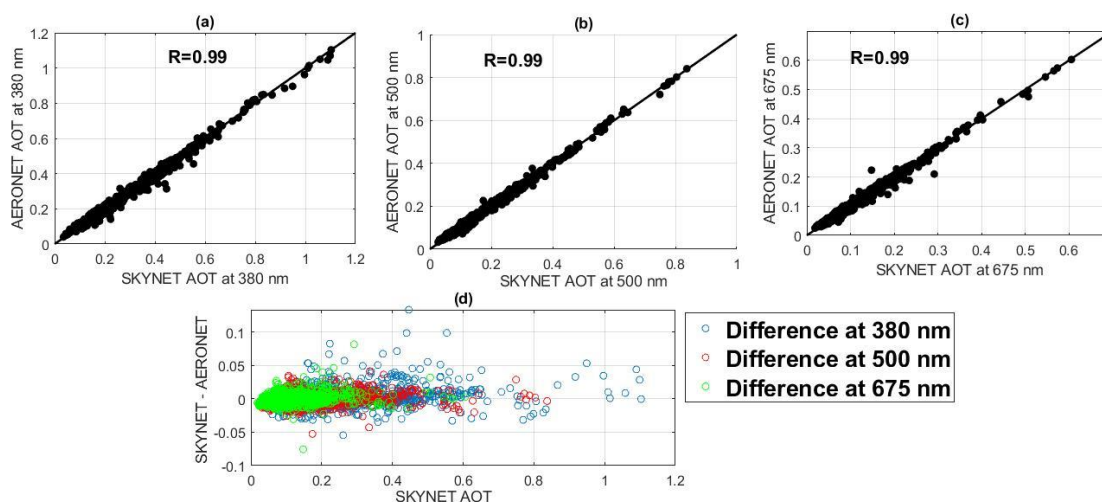


Figure 2. (top panel) Comparison between sky radiometer network (SKYNET) and aerosol robotic network (AERONET) aerosol optical thickness (AOT values) at (a) 380, (b) 500, and (c) 675 nm. The data with cloud flag 0 in both datasets were plotted. The solid black lines in (a–c) indicate the 1:1 line. (bottom panel) (d) The difference between the SKYNET and AERONET AOT values at 380, 500, and 675 nm was plotted as a function of the SKYNET AOT values at the respective wavelengths.

Table 6. Summary statistics of the comparison between SKYNET and AERONET AOT at 380 nm at the Chiba site.

Wavelength (nm)	SKYNET		AERONET		Number of Data Points	Correlation Coefficient (R)	Slope
	Mean	SD	Mean	SD			
380	0.31	0.18	0.3	0.18	1782	0.99	0.996
500	0.18	0.11	0.18	0.11	1061	0.99	0.997
675	0.11	0.07	0.11	0.07	1061	0.99	0.993

3.3.2. Sky Radiometer and MAX-DOAS Observations in Phimai

Coincident AERONET observations were not available for the Phimai site. Thus, the sky radiometer AOT values in Phimai were compared with the aerosol dataset from coincident MAX-DOAS observations. Figure 3 shows the AOT at 476 nm retrieved from the sky radiometer and MAX-DOAS observations in Phimai. The sky radiometer AOT values at 500 nm were converted to those at 476 nm using the sky radiometer Angstrom exponent (AE) data. Coincident days with at least four observations were selected. The statistics of the comparison are shown in Table 7. The sky radiometer and MAX-DOAS AOT values at 476 nm showed good agreement with an R -value of 0.73. In some cases, larger differences were observed between the sky radiometer and MAX-DOAS values at 476 nm. The integration times of the two instruments differed. It was unlikely that the difference in integration time was the dominant factor driving the differences in the AOT values. Another possible cause was the impact of clouds. An example case using LIDAR observations in Phimai is shown in Figure 3. Figure 3d,e show coincident LIDAR measurements in Phimai for some selected days in April and August 2019. On April 23, 24, and 25, the attenuated backscatter coefficient was low, indicating clear sky conditions. On August 21 and 22, clouds (high backscatter coefficient) were observed. The differences in the AOT values on these days are shown in Figure 3c. On clear sky days, the differences in the AOT values were lower. When clouds were present, the differences in the two observations were greater, especially for low-altitude clouds. Thus, differences could occur if clouds

were not properly screened. Despite these differences, sky radiometer and MAX-DOAS observations at both sites showed good agreement under clear sky conditions.

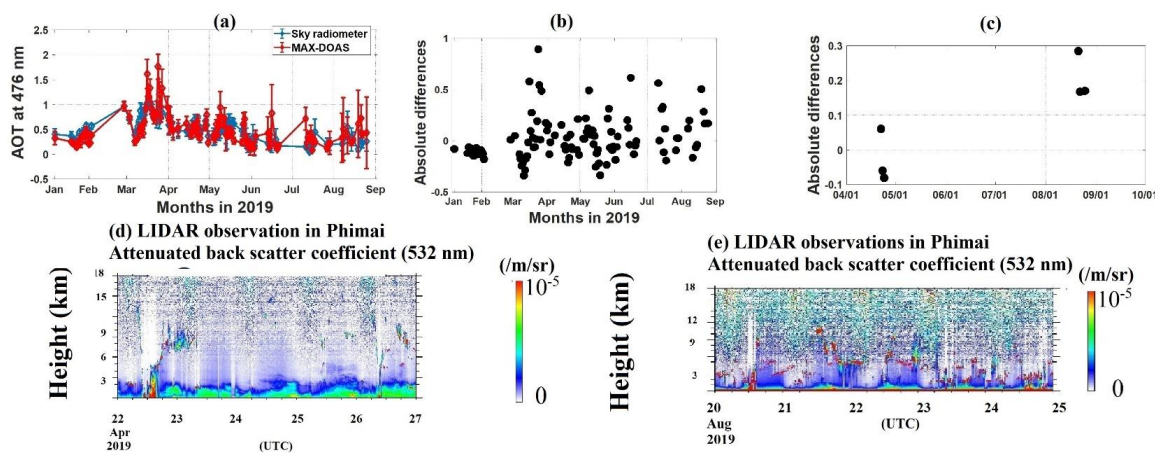


Figure 3. (top panel) (a) Sky radiometer and MAX-DOAS AOT at 476 nm retrieved from the observations in Phimai, (b) The absolute differences between MAX-DOAS and sky radiometer AOT at 476 nm in Phimai. (c) The absolute differences between MAX-DOAS and sky radiometer AOT at 476 nm on April 23, 24, and 25 and August 21 and 22. (bottom panel) Coincident LIDAR observations at the Phimai site on (d) April 23, 24, and 25 and (e) August 21 and 22. The LIDAR images were obtained from the NIES LIDAR website (<https://www-lidar.nies.go.jp/Phimai/archives/>, last access 2020/7/15).

Table 7. Summary statistics for the sky radiometer and MAX-DOAS observations in Phimai. All the coincident data for the observation period were used to calculate the mean values.

Sky Radiometer AOT at 476 nm	MAX-DOAS AOT at 476 nm	Number of Data	Mean Bias Error (Sky Radiometer–MAX-DOAS)	Correlation Coefficient (R)
0.57 ± 0.31	0.54 ± 0.26	109	0.02	0.73

4. Results

4.1. Evaluation of GCOM-C Data

Scatter plots of AOT at 380 nm retrieved from GCOM-C and sky radiometer observations in Chiba and Phimai are illustrated in Figure 4. The days of overlap between GCOM-C and sky radiometer data were analyzed. Sky radiometer data within ±20 min of the satellite overpass time were selected. Satellite data within a 30 km radius of the observation sites were compared. The observation time and satellite observation radius were optimized to obtain sufficient coincident points for comparison. As the Chiba site is situated near the sea, only the data over land were selected using the land-sea mask information. The number of coincident points available for the Chiba and Phimai site was 47 and 31, respectively.

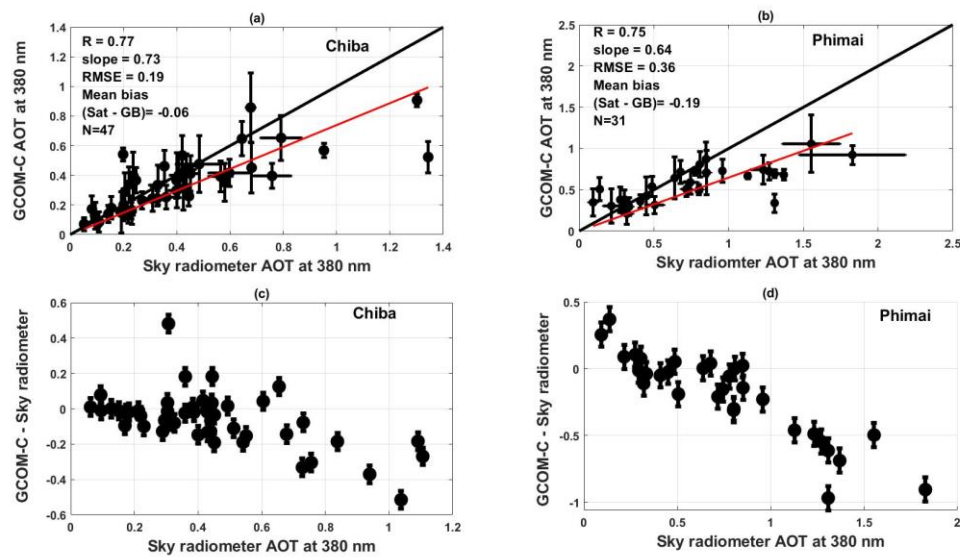


Figure 4. (top panel) The scatter plot of the sky radiometer and GCOM-C AOT at 380 nm at (a) Chiba and (b) Phimai. The GCOM-C data within 30 km centered on the sites were selected for the comparison. Only the clear sky day (based on the GCOM-C cloud flag) data are shown. For the Chiba site, GCOM-C data only over land was selected using the land-sea mask information. The red lines in the scatter plots are the least square fitted lines to the scatter plots. The black lines indicate the 1:1 line. The error bars indicate the 1σ standard deviation. (bottom panel) (c) The absolute differences between the coincident sky radiometer and GCOM-C observations at (c) Chiba and (d) Phimai. The error bars in (c,d) indicate the standard error in the differences. N indicates the number of coincident samples available for the comparison.

A good positive correlation (R) of 0.77 and 0.75 at Chiba and Phimai, respectively, was observed. Figure 4c,d show the absolute differences between GCOM-C and sky radiometer observations over both sites. At both sites, the AOT values mostly agreed within ± 0.2 , and the differences larger than ± 0.2 were observed mostly at higher AOT values. One potential reason for these larger differences could be the influence of clouds. At Chiba, the difference ~ 0.39 was observed on 22 April (Table 8). The coincident sky camera images showed clouds around the GCOM-C overpass time on 22 April (<http://atmos3.cr.chiba-u.jp/skyview/svchib201904.html>; last accessed on 13 February 2020). Similarly, a few clouds were observed during the GCOM-C overpass time on March 8 (<http://atmos3.cr.chiba-u.jp/skyview/svchib201903.html>; last accessed on 13 February 2020). However, the agreement between the two datasets was very good on 8 March (Table 8). Although both datasets were subjected to cloud screening schemes, some cloud pixels might not have been removed, which could lead to the differences observed on 22 April.

Table 8. The sky radiometer and GCOM-C AOT on some selected days at the Chiba site.

Date	Sky Radiometer AOT	GCOM-C AOT	AOT Difference
22 April 2019	0.93	0.56	0.39
8 March 2019	0.12	0.12	0

The mean bias error (MBE) values in Chiba and Phimai were -0.06 and -0.19 , respectively, for the coincidence criterion of 30 km around the sites. Table 9 shows the estimated MBE, root mean square error (RMSE), slope, and R -values, at both sites, for GCOM-C data of various spatial resolutions.

Table 9. The MBE, RMSE, slope, and R calculated for the different spatial resolution of the GCOM-C observations. The parameters were calculated for both wavelengths in Chiba and Phimai. The number of data points (N) for each coincidence criterion for both sites is also shown.

Site	Parameter	≤10 km	≤20 km	≤40 km	≤50 km	≤70 km	≤90 km
Chiba	MBE	−0.02	−0.04	−0.07	−0.07	−0.08	−0.08
	RMSE	0.17	0.16	0.17	0.18	0.22	0.22
	Slope	0.88	0.83	0.78	0.77	0.7	0.7
	R	0.73	0.76	0.78	0.78	0.62	0.6
	N	41	42	47	48	54	56
Phimai	MBE	−0.19	−0.19	−0.20	−0.20	−0.20	−0.21
	RMSE	0.36	0.36	0.37	0.36	0.38	0.39
	Slope	0.65	0.64	0.63	0.62	0.61	0.6
	R	0.78	0.75	0.73	0.71	0.7	0.69
	N	28	30	33	33	34	34

At both sites, MBE didn't change significantly with changes in the spatial resolution of the satellite coincidence point. At Chiba, the R -values were almost similar for the satellite coincidence point less than 50 km around the Chiba site. This indicated the good performance of GCOM-C retrievals at 380 nm over heterogeneous surfaces. The MBE values at Phimai were higher compared to those of Chiba, irrespective of the GCOM-C coincidence criterion. The potential reasons for the MBE and differences between the datasets are discussed in the later sections.

4.2. Potential Reasons for the Differences in the AOT Values other than Cloud Influence

4.2.1. Aerosol Composition in Chiba

The changes in the aerosol composition could impact the observed differences in the dataset. To investigate the aerosol types in Chiba, AE, AAE, EAE, and aerosol volume size distribution data were analyzed. AAE values were calculated following the procedure of Irie et al. [18], using the following equations

$$\ln[AAOD(\lambda)] = a - AAE \times \ln(\lambda) \quad (3)$$

$$AAOD(\lambda) = AOD(\lambda) \times [1 - SSA(\lambda)] \quad (4)$$

EAE values were calculated as the slope of the linear fit of $\ln[AOT]$ versus $\ln[\lambda]$

$$\ln[AOD(\lambda)] = a - EAE \times \ln(\lambda) \quad (5)$$

where a is the intercept in Equations (3) and (5). The wavelength ranges from 340–870 nm were used for the calculation. Aerosol volume size distribution data were obtained from the coincident AERONET sunphotometer measurements. The aerosol volume size distribution retrieved using SR-CEReS is not yet well understood. The coincident AERONET volume size distribution data were used as supporting information along with sky radiometer observations to infer aerosol composition in Chiba. Figure 5 shows AE, AAE, and EAE values, as well as the mean aerosol volume size distribution for the observation period in Chiba. The aerosol mean volume size distribution was shown for coincident days between the SKYNET and AERONET observations. The AE values are generally greater than 1, indicating that small particles are dominant. The mean size distribution also showed that fine-mode aerosols were dominant in Chiba. AAE values range between 1 and 2, with values between 1 and 1.5 representing dominant urban-industrial aerosols, larger values ($\sim >1.5$) representing biomass burning aerosols, and the largest values ($\sim >2.00$) representing dust aerosols [54]. AAE values between 1.2 and 1.5 occurred with the highest frequency during the observation period in Chiba. The observed AAE values (1.2–1.5) were in the range reported by Russel et al. [54] for dominant urban-industrial aerosols. However, the upper limit of the AAE range (i.e., 1.5) was similar to the AAE value (1.57) for dominant

biomass burning aerosols reported by Irie et al. [18]; however, while they reported values over their entire observation period, the values reported in this work were daily mean AAE values.

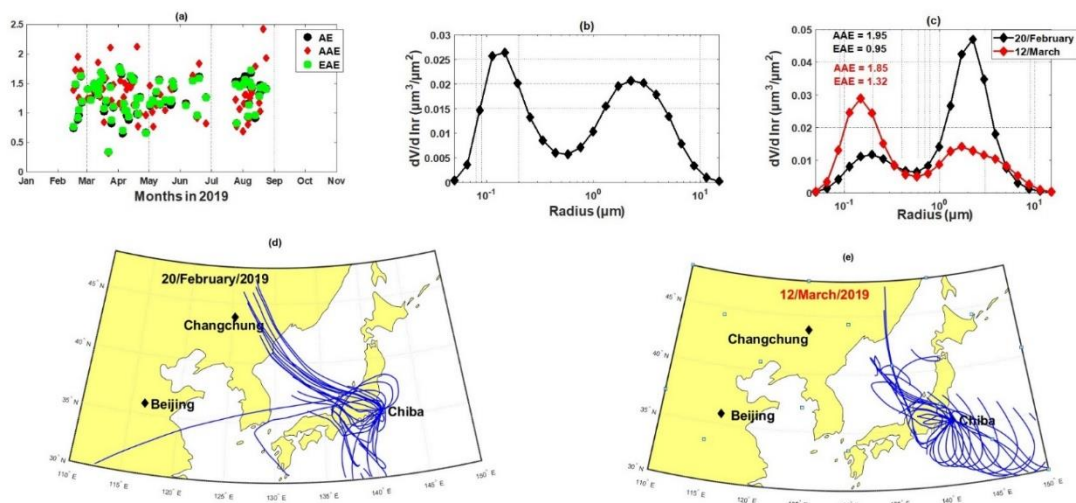


Figure 5. (top panel) (a) The Angstrom exponent (AE), absorption Angstrom exponent (AAE), and extinction Angstrom exponent (EAE) values in Chiba for the observation period. The AAE and EAE values were calculated using Equations (1) and (2). (b) The mean aerosol volume size distribution for the observation period. The volume size distribution data from the coincident AERONET observations were used. Only the coincident days between the SKYNET and AERONET observations were used in the calculation. (c) The aerosol volume size distribution for 20 February and 12 March. The days were selected based on AAE values. (bottom panel) (d) 48 h backward trajectories, starting from 200 m above ground level over the Chiba site on February 20, 2019. (e) Similar 48 h backward trajectory on 12 March 2019.

On some days, AAE values were as high as ~ 2 , which fell within the range of AAE values for dominant dust aerosols reported by Russel et al. [54]. Figure 5 shows a case (February 20) when the AAE value was 1.95. The aerosol volume size distributions, EAE values, and 48-h backward trajectories of air masses at the height of 200 m arriving in Chiba are depicted in Figure 5d,e. The backward trajectories were calculated using the HYSPLIT model [55]. The EAE value on February 20 was < 1 , indicating the presence of larger particles in the air. Aerosol volume size distribution data also supported the presence of larger particles on that day (Figure 5c). Backward trajectories showed that air masses from the Changchun area in China, where sand fields are located [56], arrived at the Chiba site. Moreover, the weather in Harbin city (located near Changchun) is often affected by sand and dust from Northwest China and Inner Mongolia [57]. This result indicated that dust particles were transported to the Chiba site.

However, a high AAE value did not necessarily indicate the presence of dust aerosols in Chiba. The AAE, EAE, aerosol volume size distribution, and 48-h backward trajectories on March 12 are shown in Figure 5; on that date, the AAE and EAE values were 1.85 and 1.32, respectively. Besides, the aerosol volume size distribution on that date showed that fine-mode aerosols were dominant in Chiba. The trajectories also showed that no dust was transported to the site on 12 March. However, the EAE value on March 12 was high, indicating the dominance of fine-mode aerosols. In most cases, the presence of dominant coarse-mode aerosols was noted when the EAE value was $< \sim 1$. Moreover, the transport of dust was infrequent, despite air masses regularly arriving from the Changchun region. Thus, interpreting the aerosol composition in Chiba using one parameter (i.e., AAE or EAE) might lead to incorrect conclusions. Thus, multiple variables (EAE, AAE, and aerosol volume size distribution) were used to interpret information on aerosol composition.

4.2.2. Impact of Aerosol Composition Change on the Observed Differences in the Datasets in Chiba

Figure 6 shows the sky radiometer and GCOM-C AOT, AE values, and aerosol size distribution on days with different aerosol composition. Three coincident days were selected based on AAE and EAE values, as well as the aerosol volume size distribution. On April 5, dust was transported to the Chiba site, as supported by the AAE and EAE values and the volume size distribution. The AE values in both datasets showed good agreement despite the large uncertainties in GCOM-C AE values. On April 5, both sky radiometer and GCOM-C observations showed high AOT values, compared to the other two days. This indicated the GCOM-C observations were able to capture the presence of dust on April 5, despite the differences in the absolute AOT values. On April 4, the AOT values in both datasets didn't agree within the error ranges, despite a good agreement in the AE values. Figure 6c shows the differences in the AOT values as a function of differences in the AE values. The differences in the AOT values didn't show any clear dependence on the differences in the AE values. Thus, it is unlikely that the impact of changes in the aerosol composition would have a significant impact on the differences in the AOT values.

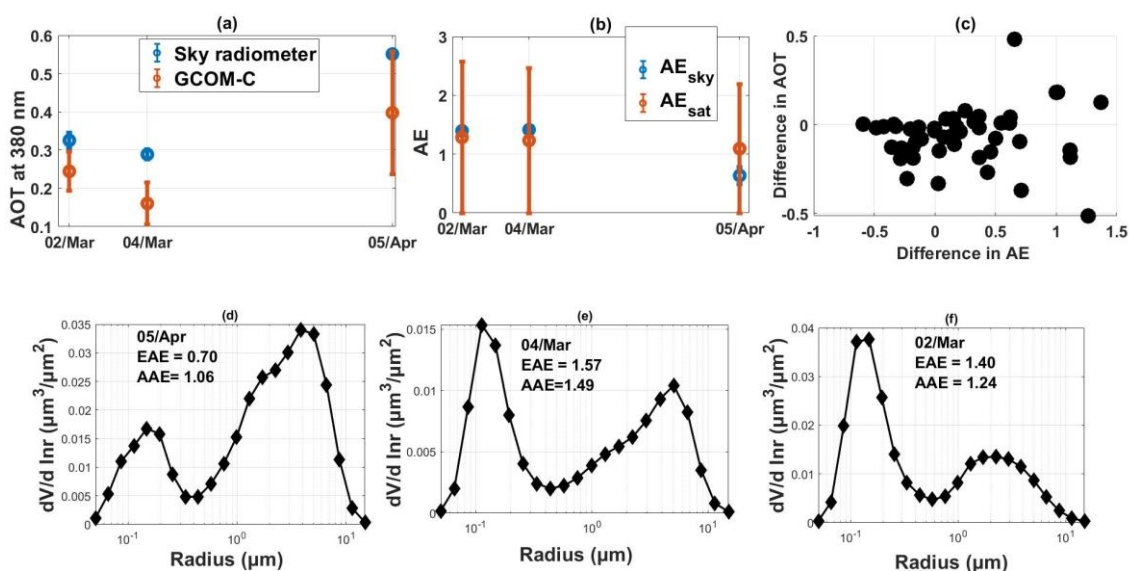


Figure 6. (top panel) (a) The sky radiometer and GCOM-C AOT at 380 in Chiba on March 2 and 4 and April 5. The coincident days were selected based on the AAE, EAE, and volume size distribution data. (b) The corresponding sky radiometer and GCOM-C AE values on March 2 and 4 and April 5. The sky radiometer and GCOM-C AE are denoted as AE_{sky} and AE_{sat} , respectively. (c) The difference between the sky radiometer and GCOM-C AOT was plotted as a function of differences in AE_{sky} and AE_{sat} . (bottom panel) The aerosol volume size distribution from the coincident AERONET observations in Chiba on (d) April 5, (e) 4 March, and (f) March 2. The example days were chosen based on the AAE and EAE values.

4.2.3. Biomass Burning Influence at the Phimai Site

According to Figure 7a, larger differences in AOT values in Phimai occurred primarily from March to May. In Phimai, the periods from January to April and July to September are considered the dry and wet seasons, respectively [22]. During the dry season, the Phimai site is influenced by biomass burning, which has been described in detail in several studies [22,58,59]. The mean AAE value during

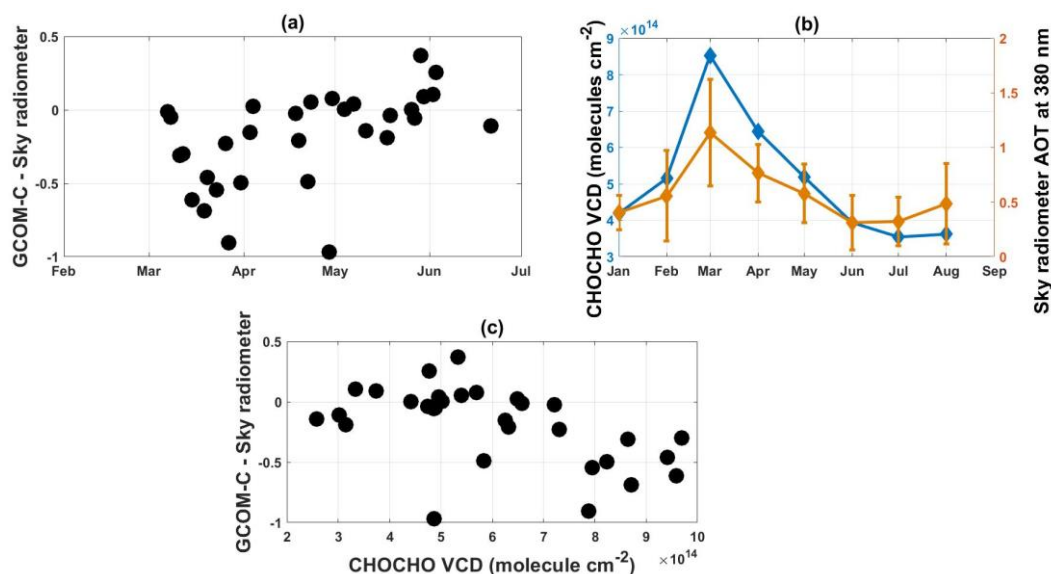


Figure 7. (top panel) (a) The time series of the difference between the GCOM-C and sky radiometer AOT at 380 nm in Phimai. (b) The seasonal variation of the glyoxal (CHOCHO) vertical column density (VCD) and the sky radiometer AOT values at 380 nm. The CHOCHO VCDs were retrieved from the MAX-DOAS observations using the JM2 algorithm. The error bars show the 1σ standard deviation of the mean values. (bottom panel) (c) The difference between coincidence GCOM-C and sky radiometer at 380 nm plotted as a function of CHOCHO VCD values. CHOCHO VCD values for the day prior to the coincident date between MAX-DOAS, sky radiometer, and GCOM-C were plotted.

The dry season in Phimai was 1.57, which lied within the range of dominant biomass burning aerosols [18]. Figure 7b shows the seasonal variations in AOT values at 380 nm and glyoxal (CHOCHO) levels at Phimai. CHOCHO, which is predominantly an oxidation product of biogenic volatile organic carbons, can also be emitted from biomass burning and biofuel use [60]. Strong agreement between CHOCHO and fire radiative power (FRP) has been reported in the region, where CHOCHO sources are predominantly pyrogenic [61]. Figure 7b also shows good agreement between the seasonality of CHOCHO VCD and sky radiometer AOT values at 380 nm. This result indicated that higher AOT values mostly occurred during the dry season due to the influence of biomass burning. Figure 7c also shows differences in AOT values at 380 nm as a function of CHOCHO VCD. CHOCHO VCD values for the day prior to the coincident date between MAX-DOAS, sky radiometer, and GCOM-C observations were used to construct Figure 7c. The influence of biomass burning at Phimai depends on the fire intensity (i.e., FRP), location of burning, and movement of air masses to the site. Based on CHOCHO data obtained around the time of GCOM-C overpass, the influence of biomass burning might not be well captured, as the time of fire occurrence was unknown. CHOCHO data with a lag of 1 day was more likely to capture the biomass burning effect. According to Figure 7c, some large differences in AOT values at 380 nm were associated with high CHOCHO VCD values. This means the large differences in the AOT values mostly occurred during the intense biomass burning period. An example using FRP and backward trajectories is shown in Figure 8.

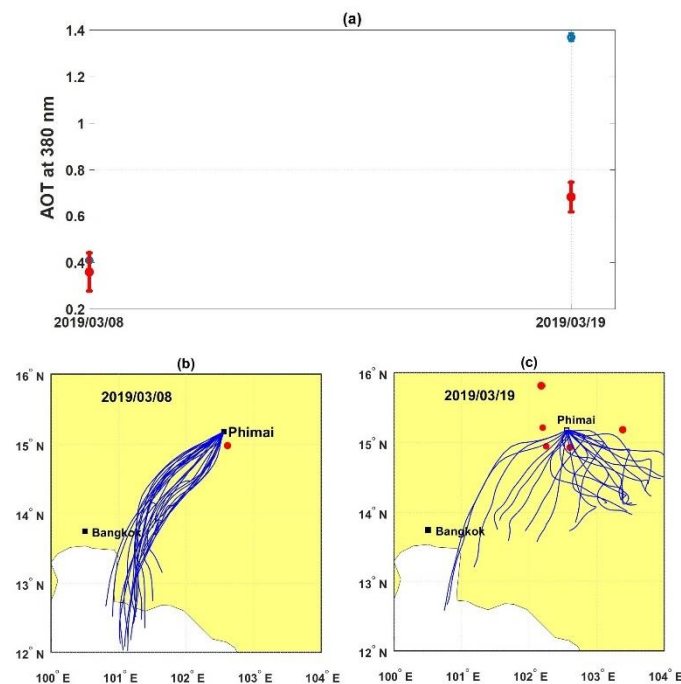


Figure 8. (a) The sky radiometer and GCOM-C AOT values at 380 nm in Phimai on March 8 and 19. The error bars indicate the 1σ standard deviation. 24 h backward trajectories, starting from 200 m above ground level over the Phimai site on (b) March 8 and (c) March 19, 2019. The red dots indicate the fire activities within 100 km of the Phimai site.

Figure 8 shows the fire hotspots within a 100-km radius of the Phimai site and 24-h backward trajectories of air masses arriving at Phimai at the height of 200 m on March 8 and 19. FRP data (MODIS collection 6) were extracted from the MODIS active fire detections dataset distributed by NASA FIRMS (<https://firms.modaps.eosdis.nasa.gov>). The backward trajectories were calculated using the HYSPLIT model. On March 19, the difference between GCOM-C and sky radiometer AOT values at 380 nm was -0.69 . The mean FRP on March 19 was $\sim 84 \text{ Wm}^{-2}$. The air masses arriving in Phimai had traveled over regions of fire activity. Thus, a strong influence of biomass burning was observed at the Phimai site on March 19. On March 8, a few fire hotspots were detected around Phimai. As the air masses present on March 8 had barely passed over any area of fire activity, the impact of fires at the site was low, and the difference between datasets was -0.04 . This indicated that, in addition to clouds, biomass burning had a significant impact on the observed differences in the observed AOT values in Phimai.

4.3. Diurnal Variation of AOT at 380 nm Inferred from GCOM-C and OMI Observations

The difference in the GCOM-C (10:30 LT) and OMI (13:30 LT) overpass time could be used to study the diurnal variations in AOT at 380 nm. The OMI UV aerosol products were provided at 388 nm, which was similar to the wavelength (i.e., 380 nm) of the sky radiometer and GCOM-C UV aerosol product. Uncertainty related to the slight difference in wavelength is expected to have a non-significant impact in the analysis; thus, the OMI AOT at 388 nm was not converted to 380 nm. However, in the text and figure, these data are referred to as AOT at 380 nm to avoid confusion and maintain consistency. Sky radiometer observations within ± 20 min of the OMI overpass time (13:30 LT) were selected. For both OMI and GCOM-C, points within a 20-km radius of the sites were used. OMI data with a cloud flag and cloud fraction of 0 and < 0.2 , respectively, were used. Figure 9 shows the diurnal variations in AOT at 380 nm over both sites on some selected coincident dates between the sky radiometer and satellite (GCOM-C + OMI) observations. In Chiba, the sky radiometer AOT values were higher compared to the morning values. Such an increase in the AOT values was also seen in the satellite (GCOM-C + OMI) observations, despite the differences in the absolute AOT values.

This indicated that quantitative information on the temporal variation of aerosols over heterogeneous surfaces could be obtained from the combination of GCOM-C and OMI datasets.

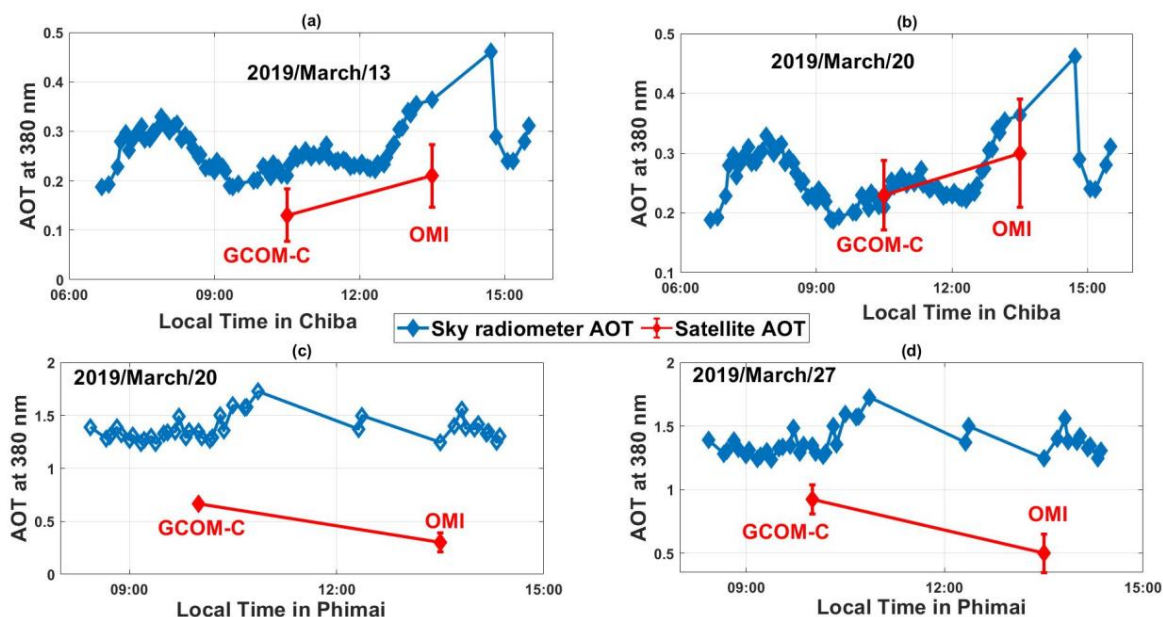


Figure 9. (top panel) The diurnal variation in the AOT at 380 inferred from the sky radiometer and combination of GCOM-C and ozone monitoring instrument (OMI) AOT values in Chiba on (a) 13 March and (b) 20 March. The sky radiometer data within 20 min of GCOM-C (10:20 LT) and OMI (13:30) overpass time were used. The coincidence criterion for both satellite dataset was within 20 km of the Chiba site. (bottom panel) The diurnal variation in AOT at 380 nm observed from the sky radiometer and combined satellite (GCOM-C plus OMI) observations in Phimai on (c) 20 March and (d) 27 March. The data selection criterion for the sky radiometer and satellites was similar to that for Chiba. The error bars in (a–d) indicate the 1σ standard deviation.

Over Phimai, the sky radiometer and satellite (GCOM-C + OMI) observations showed different diurnal variations. Moreover, large differences between satellite (GCOM-C + OMI) and sky radiometer AOT values were observed. The example dates for the Phimai site were during the dry season when the site is strongly influenced by biomass burning (discussed in the previous sections). The differences in the diurnal variations could be related to the impact of biomass burning on the observations. It would be interesting to see the agreement in the diurnal variations during the wet season when such conditions (biomass burning) don't prevail. However, no coincident dates during the wet season were available within the present datasets. This issue will be addressed in our future studies. Overall, the combination of GCOM-C and OMI observations provided a good opportunity to infer aerosol characteristics in the UV region.

5. Discussion

The Phimai site experiences biomass burning impact during the dry season. The biomass burning influence had a significant impact on the large differences in the AOT values at Phimai, in addition to cloud contamination. This was also reflected in the high MBE values in Phimai compared to Chiba for the same coincident criterion of the satellite observations. It is expected that GCOM-C and sky radiometer observation in Phimai will show better agreement during the wet season due to the absence of strong emission sources. Such a hypothesis can be tested with long term datasets for Phimai and other rural sites of SKYNET. Some potential reasons for the large differences observed in the datasets under biomass burning influence are – (1) The distance of the ground-based stations from the fire locations is shorter compared to the satellite sensors. Thus, the strong influence of the fires on the ground-station can infer large differences in the comparison results. (2) The time of

occurrence and the location of the fires are unknown and random. The optical and physical properties (size distribution, chemical composition, hygroscopicity, etc.) of biomass burning particles change considerably during the first 2–4 h of their atmospheric transport [62]. Such changes might not reflect in the satellite measurements due to the limited observation period (one measurement a day during the overpass time).

Comparing the OMI and collocated AERONET AOT at 380 nm at more than twenty-two sites, Ahn et al. [9] reported that R , RMSE, and slope values were in the range of 0.41–0.91, 0.08–0.25, and 0.33–0.92, respectively. The statistics of the comparison between SKYNET and GCOM-C are within the range of the reported values, except for the RMSE value (~ 0.35) at the Phimai site, where biomass burning influences can incur large differences in the AOT values. However, the study of Ahn et al. [9] reported RMSE value around 0.18 for sites located in the biomass burning regions. The limited number of collocated data points can be one of the potential reasons for the higher RMSE value at the Phimai site. The comparisons of Ahn et al. [9] included at least ~ 100 collocated data points over four years. Moreover, despite the high RMSE value at the Phimai site, the R and slope values were almost similar to or better in some cases than the biomass burning sites included in the study of Ahn et al. [9]. Furthermore, in the diurnal variations in AOT at Phimai (Figure 9), the difference in the GCOM-C and sky radiometer was lower compared to that of between the sky radiometer and OMI. Thus, utilizing a long-term dataset, the statistics of the comparison between GCOM-C and sky radiometer is expected to improve, and the impact of the improved spatial resolution of GCOM-C will be more evident.

In addition to the potential reasons discussed here, uncertainties in the sky radiometer inversion product may also contribute to the observed biases. For example, the solar disk scan method can underestimate the calibration constant, resulting in an overestimation of sky radiances and SSA [63]. Moreover, the different assumptions in both retrieval algorithms can also impact the differences in the AOT values.

Apart from the discussions in this work, qualitative assessment of the retrieval algorithms (i.e., different assumptions, error in the model calculations, etc.) is required to identify further potential reasons for the disagreement in the AOT values. A qualitative assessment of the GCOM-C AOT data utilizing long term datasets and including more representative ground sites will be addressed in our future study.

6. Conclusions

The newly available GCOM-C AOT at 380 nm was evaluated using sky radiometer observations at the SKYNET Chiba and Phimai sites. GCOM-C is currently the only satellite providing AOT at 380 nm during morning overpass time. The sky radiometer observations in Chiba were compared with coincident AERONET observations, and the agreement between the datasets was mostly within ± 0.02 . The sky radiometer and MAX-DOAS observations in Phimai also showed good agreement mostly under clear sky conditions. At both the sites, the agreement between the sky radiometer and GCOM-C AOT at 380 nm was mostly within ± 0.2 , with a positive correlation of ~ 0.73 . The number of coincident points for the Chiba and Phimai site was 47 and 31, respectively, for a coincidence criterion of ≤ 30 km. Larger differences in AOT values occurred at Chiba, mostly due to the effect of clouds on the observations. At times, long-range dust transport occurred at Chiba. Such a change in the aerosol composition did not show any clear impact on the differences in the AOT. The Phimai site is affected by biomass burning during the dry season. The influence of biomass burning had a significant impact on the differences observed in the datasets at the Phimai site. The difference in the overpass time of GCOM-C and OMI was utilized to study the diurnal variations in the AOT at 380 nm. The combination of GCOM-C and OMI AOT captured the diurnal variations in AOT at Chiba only. At Phimai, the coincident days among GCOM-C, OMI, and sky radiometer were only available for the dry season. Thus, the strong influence of biomass burning potentially led to the poor agreement of the diurnal variations in Phimai. Overall, the AOT values retrieved in both datasets (sky radiometer and GCOM-C) were consistent, indicating the strong potential of the GCOM-C UV AOT product.

Author Contributions: H.M.S.H. conceptualized the study, conducted the data analysis, and wrote the paper. H.I. and A.D. shared their experience to interpret the results and also helped improve the manuscript write-up. M.M. helped in the data analysis. All authors have read and agreed to the published version of the manuscript.

Funding: This research was supported by the Environmental Research and Technology Development Fund (2-1901) of the Environmental Restoration and Conversation Agency of Japan, JSPS KAKENHI (grant numbers JP19H04235 and JP17K00529), the JAXA 2nd research announcement on the Earth Observations (grant number 19RT00351), and JST CREST (grant number JPMJCR15K4).

Acknowledgments: We thank the GCOM-C scientific team for the public release of the aerosol products. We are grateful to Hiroshi Murakami of JAXA for useful comments and suggestions. Acknowledgments are also due to the National Institute for Environmental Study (NIES) LIDAR team (<https://www-lidar.nies.go.jp/AD-Net/>) and the NASA Earth Science data center, for the online availability of the LIDAR images and OMI aerosol products, respectively.

Conflicts of Interest: The authors declare no conflict of interest.

Data Availability: The sky radiometer and MAX-DOAS data used in this study can be obtained from the SKYNET website, <http://atmos3.cr.chiba-u.jp/skyenet/data.html> (last accessed on 5 March 2020). The availability of satellite data products is mentioned in the text.

References

1. Pope, C.A.; Dockery, D.W. Health Effects of Fine Particulate Air Pollution: Lines that Connect. *J. Air Waste Manag. Assoc.* **2006**, *56*, 709–742. [[CrossRef](#)] [[PubMed](#)]
2. Tao, M.; Chen, L.; Wang, Z.; Tao, J.; Su, L. Satellite observation of abnormal yellow haze clouds over East China during summer agricultural burning season. *Atmos. Environ.* **2013**, *79*, 632–640. [[CrossRef](#)]
3. IPCC. Climate Change 2013: The Physical Basis. In *Contribution of the Working Group 1 to the Fifth Assessment Report of the Intergovernmental Panel on Climate Change*; Cambridge University Press: New York, NY, USA, 2013; p. 1535.
4. Kaufman, Y.J.; Tanre, D.; Remer, L.A.; Vermote, E.F.; Chu, A.; Holben, B.N. Operational remote sensing of tropospheric aerosol over land from EOS moderate resolution imaging spectroradiometer. *J. Geophys. Res. Space Phys.* **1997**, *102*, 17051–17067. [[CrossRef](#)]
5. King, M.D.; Kaufman, Y.J.; Tanré, D.; Nakajima, T. Remote Sensing of Tropospheric Aerosols from Space: Past, Present, and Future. *Bull. Am. Meteorol. Soc.* **1999**, *80*, 2229–2259. [[CrossRef](#)]
6. Mishchenko, M.; Penner, J.; Anderson, D. Global Aerosol Climatology Project. *J. Atmos. Sci.* **2002**, *59*, 249. [[CrossRef](#)]
7. Omar, A.H.; Winker, D.M.; Vaughan, M.A.; Hu, Y.; Trepte, C.R.; Ferrare, R.A.; Lee, K.-P.; Hostetler, C.A.; Kittaka, C.; Rogers, R.R.; et al. The CALIPSO Automated Aerosol Classification and Lidar Ratio Selection Algorithm. *J. Atmos. Ocean. Technol.* **2009**, *26*, 1994–2014. [[CrossRef](#)]
8. Torres, O.; Tanskanen, A.; Veihelmann, B.; Ahn, C.; Braak, R.; Bhartia, P.K.; Veefkind, P.; Levelt, P. Aerosols and surface UV products from Ozone Monitoring Instrument observations: An overview. *J. Geophys. Res. Space Phys.* **2007**, *112*, 24. [[CrossRef](#)]
9. Ahn, C.; Torres, O.; Jethva, H. Assessment of OMI near-UV aerosol optical depth over land. *J. Geophys. Res. Atmos.* **2014**, *119*, 2457–2473. [[CrossRef](#)]
10. Kirchstetter, T.W.; Novakov, T.; Hobbs, P.V. Evidence that the spectral dependence of light absorption by aerosols is affected by organic carbon. *J. Geophys. Res. Space Phys.* **2004**, *109*, 21208. [[CrossRef](#)]
11. Saleh, R.; Robinson, E.S.; Tkacik, D.S.; Ahern, A.T.; Liu, S.; Aiken, A.C.; Sullivan, R.C.; Presto, A.A.; Dubey, M.K.; Yokelson, R.J.; et al. Brownness of organics in aerosols from biomass burning linked to their black carbon content. *Nat. Geosci.* **2014**, *7*, 647–650. [[CrossRef](#)]
12. Torres, O.; Bhartia, P.K.; Herman, J.R.; Ahmad, Z.; Gleason, J. Derivations of aerosol optical properties from satellite measurements of backscattered ultraviolet radiation: Theoretical basis. *J. Geophys. Res.* **1998**, *103*, 23321. [[CrossRef](#)]
13. Torres, O.; Bhartia, P.K.; Herman, J.R.; Sinyuk, A.; Ginoux, P.; Holben, B. A Long-Term Record of Aerosol Optical Depth from TOMS Observations and Comparison to AERONET Measurements. *J. Atmos. Sci.* **2002**, *59*, 398–413. [[CrossRef](#)]

14. Torres, O.; Bhartia, P.K.; Sinyuk, A.; Welton, E.J.; Holben, B. Total Ozone Mapping Spectrometer measurements of aerosol absorption from space: Comparison to SAFARI 2000 ground-based observations. *J. Geophys. Res. Space Phys.* **2005**, *110*, 10. [[CrossRef](#)]
15. Jethva, H.; Torres, O.; Ahn, C. Global assessment of OMI aerosol single-scattering albedo using ground-based AERONET inversion. *J. Geophys. Res. Atmos.* **2014**, *119*, 9020–9040. [[CrossRef](#)]
16. Ahn, C.; Torres, O.; Bhartia, P.K. Comparison of Ozone Monitoring Instrument UV Aerosol Products with Aqua/Moderate Resolution Imaging Spectroradiometer and Multiangle Imaging Spectroradiometer observations in 2006. *J. Geophys. Res. Space Phys.* **2008**, *113*, 16. [[CrossRef](#)]
17. Holben, B.; Eck, T.; Slutsker, I.; Tanre, D.; Buis, J.; Setzer, A.; Vermote, E.; Reagan, J.; Kaufman, Y.; Nakajima, T.; et al. AERONET—A Federated Instrument Network and Data Archive for Aerosol Characterization. *Remote Sens. Environ.* **1998**, *66*, 1–16. [[CrossRef](#)]
18. Irie, H.; Hoque, H.M.S.; Damiani, A.; Okamoto, H.; Fatmi, A.M.; Khatri, P.; Takamura, T.; Jarupongsakul, T. Simultaneous observations by sky radiometer and MAX-DOAS for characterization of biomass burning plumes in central Thailand in January–April 2016. *Atmos. Meas. Tech.* **2019**, *12*, 599–606. [[CrossRef](#)]
19. Hönninger, G.; Von Friedeburg, C.; Platt, U. Multi axis differential optical absorption spectroscopy (MAX-DOAS). *Atmos. Chem. Phys. Discuss.* **2004**, *4*, 231–254. [[CrossRef](#)]
20. Irie, H.; Nakayama, T.; Shimizu, A.; Yamazaki, A.; Nagai, T.; Uchiyama, A.; Zaizen, Y.; Kagamitani, S.; Matsumi, Y. Evaluation of MAX-DOAS aerosol retrievals by coincident observations using CRDS, lidar, and sky radiometer in Tsukuba, Japan. *Atmos. Meas. Tech. Discuss.* **2015**, *8*, 1013–1054. [[CrossRef](#)]
21. Yoshida, M.; Kikuchi, M.; Nagao, T.M.; Murakami, H.; Nomaki, T.; Higurashi, A. Common Retrieval of Aerosol Properties for Imaging Satellite Sensors. *J. Meteorol. Soc. Jpn.* **2018**, 193–209. [[CrossRef](#)]
22. Hoque, H.M.S.; Irie, H.; Damiani, A. First MAX-DOAS Observations of Formaldehyde and Glyoxal in Phimai, Thailand. *J. Geophys. Res. Atmos.* **2018**, *123*, 9957–9975. [[CrossRef](#)]
23. Hori, M.; Murakami, H.; Miyazaki, R.; Honda, Y.; Nasahara, K.; Kajiwara, K.; Nakajima, T.Y.; Irie, H.; Toratani, M.; Hirawake, T.; et al. GCOM-C Data Validation Plan for Land, Atmosphere, Ocean, and Cryosphere. *Trans. Jpn. Soc. Aeronaut. Space Sci. Aerosp. Technol. Jpn.* **2018**, *16*, 218–223. [[CrossRef](#)]
24. Imaoka, K.; Kachi, M.; Fujii, H.; Murakami, H.; Hori, M.; Ono, A.; Igarashi, T.; Nakagawa, K.; Oki, T.; Honda, Y.; et al. Global Change Observation Mission (GCOM) for Monitoring Carbon, Water Cycles, and Climate Change. *Proc. IEEE* **2010**, *98*, 717–734. [[CrossRef](#)]
25. Letu, H.; Ishimoto, H.; Riedi, J.; Nakajima, T.Y.; C.-Labonnote, L.; Baran, A.J.; Nagao, T.M.; Sekiguchi, M. Investigation of ice particle habits to be used for ice cloud remote sensing for the GCOM-C satellite mission. *Atmos. Chem. Phys. Discuss.* **2016**, *16*, 12287–12303. [[CrossRef](#)]
26. Mukai, S.; Sano, I. Retrieval algorithm for atmospheric aerosols based on multi-angle viewing of ADEOS/POLDER. *Earth Planets Space* **1999**, *51*, 1247–1254. [[CrossRef](#)]
27. Torres, O.; Bhartia, P.K.; Herman, J.R.; Gleason, J.; Ahmad, Z. Derivation of aerosol properties from satellite measurements of backscattered ultraviolet radiation: Theoretical basis. *J. Geophys. Res.* **1998**, *103*, 17099–17110. [[CrossRef](#)]
28. Nakajima, T.Y.; Tsuchiya, T.; Ishida, H.; Matsui, T.N.; Shimoda, H. Cloud detection performance of space borne visible-to-infrared multispectral imagers. *Appl. Opt.* **2011**, *50*, 2601–2616. [[CrossRef](#)]
29. Letu, H.; Nakajima, T.Y.; Matsui, T.N. Development of an ice crystal scattering database for the global change observation mission/second generation global imager satellite mission: Investigating the refractive index grid system and potential retrieval error. *Appl. Opt.* **2012**, *51*, 6172–6178. [[CrossRef](#)]
30. Nakajima, T.; Tanaka, M. Matrix formulations for the transfer of solar radiation in a plane-parallel scattering atmosphere. *J. Quant. Spectrosc. Radiat. Transf.* **1986**, *35*, 13–21. [[CrossRef](#)]
31. Nakajima, T.; Tanaka, M. Algorithms for radiative intensity calculations in moderately thick atmospheres using a truncation approximation. *J. Quant. Spectrosc. Radiat. Transf.* **1988**, *40*, 51–69. [[CrossRef](#)]
32. Stamnes, K.; Tsay, S.-C.; Wiscombe, W.; Jayaweera, K. Numerically stable algorithm for discrete-ordinate-method radiative transfer in multiple scattering and emitting layered media. *Appl. Opt.* **1988**, *27*, 2502–2509. [[CrossRef](#)] [[PubMed](#)]
33. Omar, A.H.; Won, J.; Winker, D.M.; Yoon, S.; Dubovik, O.; McCormick, M.P. Development of global aerosol models using cluster analysis of Aerosol Robotic Network (AERONET) measurements. *J. Geophys. Res. Space Phys.* **2005**, *110*. [[CrossRef](#)]

34. Sayer, A.; Smirnov, A.; Hsu, N.C.; Holben, B.N. A pure marine aerosol model, for use in remote sensing applications. *J. Geophys. Res. Space Phys.* **2012**, *117*, 117. [[CrossRef](#)]
35. Nakajima, T.; Tanaka, M.; Yamano, M.; Shiobara, M.; Arao, K.; Nakanishi, Y. Aerosol Optical Characteristics in the Yellow Sand Events Observed in May, 1982 at Nagasaki-Part II Models. *J. Meteorol. Soc. Jpn.* **1989**, *67*, 279–291. [[CrossRef](#)]
36. Ishida, H.; Nakajima, T.Y. Development of an unbiased cloud detection algorithm for a spaceborne multispectral imager. *J. Geophys. Res. Space Phys.* **2009**, *114*, 7. [[CrossRef](#)]
37. Ishida, H.; Nakajima, T.Y.; Yokota, T.; Kikuchi, N.; Watanabe, H. Investigation of GOSAT TANSO-CAI Cloud Screening Ability through an Intersatellite Comparison. *J. Appl. Meteorol. Clim.* **2011**, *50*, 1571–1586. [[CrossRef](#)]
38. Rodgers, C.D. *Inverse Methods for Atmospheric Sounding: Theory and Practice*; Scientific World: Singapore, 2000.
39. Torres, O.; Ahn, C.; Chen, Z. Improvements to the OMI near-UV aerosol algorithm using A-train CALIOP and AIRS observations. *Atmos. Meas. Tech.* **2013**, *6*, 3257–3270. [[CrossRef](#)]
40. Torres, O.; Bhartia, P.K.; Jethva, H.; Ahn, C. Impact of the ozone monitoring instrument row anomaly on the long-term record of aerosol products. *Atmos. Meas. Tech.* **2018**, *11*, 2701–2715. [[CrossRef](#)]
41. Jethva, H.; Torres, O. Satellite-Based evidence of wavelength-dependent aerosol absorption in biomass burning smoke inferred from Ozone Monitoring Instrument. *Atmos. Chem. Phys.* **2012**, *11*, 10541–10551. [[CrossRef](#)]
42. Mok, J.; Krotkov, N.A.; Torres, O.; Jethva, H.; Li, Z.; Kim, J.; Koo, J.; Go, S.; Irie, H.; Labow, G. Comparisons of spectral aerosol single scattering albedo in Seoul, South Korea. *Atmos. Meas. Tech.* **2018**, *11*, 2295–2311. [[CrossRef](#)]
43. Hashimoto, M.; Nakajima, T.; Dubovik, O.; Campanelli, M.; Che, H.; Khatri, P.; Takamura, T.; Pandithurai, G. Development of a new data-processing method for SKYNET sky radiometer observations. *Atmos. Meas. Tech.* **2012**, *5*, 2723–2737. [[CrossRef](#)]
44. Campanelli, M.; Estellés, V.; Tomasi, C.; Nakajima, T.; Malvestuto, V.; Martinez-Lozano, J.A. Application of the SKYRAD Improved Langley plot method for the in situ calibration of CIMEL Sun-sky photometers. *Appl. Opt.* **2007**, *46*, 2688–2702. [[CrossRef](#)] [[PubMed](#)]
45. Nakajima, T.; Tonna, G.; Rao, R.; Boi, P.; Kaufman, Y.; Holben, B. Use of sky brightness measurements from ground for remote sensing of particulate polydispersions. *Appl. Opt.* **1996**, *35*, 2672. [[CrossRef](#)] [[PubMed](#)]
46. Uchiyama, A.; Matsunaga, T.; Yamazaki, A. The instrument constant of sky radiometers (POM-02), Part II: Solid view angle 2. *Atmos. Meas. Tech.* **2018**, *11*, 5389–5402. [[CrossRef](#)]
47. Khatri, P.; Takamura, T. An Algorithm to Screen Cloud-Affected Data for Sky Radiometer Data Analysis. *J. Meteorol. Soc. Jpn.* **2009**, *87*, 189–204. [[CrossRef](#)]
48. Kurucz, R.L. *Solar Flux Atlas from 296 to 1300 nm*; National Solar Observatory: Sunspot, NM, USA, 1984; Volume 240.
49. Irie, H.; Takashima, H.; Kanaya, Y.; Boersma, K.F.; Gast, L.; Wittrock, F.; Brunner, D.; Zhou, Y.; Van Roozendaal, M. Eight-component retrievals from ground-based MAX-DOAS observations. *Atmos. Meas. Tech.* **2011**, *4*, 1027–1044. [[CrossRef](#)]
50. Platt, U.; Stutz, J. *Dirrefential Optical Absorption Spectroscopy*; Springer: Berlin/Heidelberg, Germany, 2008.
51. Irie, H.; Kanaya, Y.; Akimoto, H.; Iwabuchi, H.; Shimizu, A.; Aoki, K. First retrieval of tropospheric aerosol profiles using MAX-DOAS and comparison with lidar and sky radiometer measurements. *Atmos. Chem. Phys. Discuss.* **2008**, *8*, 341–350. [[CrossRef](#)]
52. Irie, H.; Kanaya, Y.; Akimoto, H.; Tanimoto, H.; Wang, Z.; Gleason, J.F.; Bucsela, E.J. Validation of OMI tropospheric NO₂ column data using MAX-DOAS measurements deep inside the North China Plain in June 2006. *Atmos. Chem. Phys. Discuss.* **2008**, *8*, 8243–8271. [[CrossRef](#)]
53. Giles, D.M.; Sinyuk, A.; Sorokin, M.G.; Scafer, J.S.; Smirnov, A.; Slutsker, I.; Eck, T.F.; Holben, B.N.; Lewis, J.R.; Campbell, J.R.; et al. Advancement in the Aerosol Robotic Network (AERONET) Versiom 3 database-automated near-real-time quality control algorithm with improved cloud screening for Sun photometer aerosol optical depth (AOD) measurements. *Atmos. Chem. Phys.* **2019**, *12*, 169–209.
54. Russell, P.B.; Bergstrom, R.W.; Shinozuka, Y.; Clarke, A.D.; Decarlo, P.F.; Jimenez, J.L.; Livingston, J.M.; Redemann, J.; Dubovik, O.; Strawa, A. Absorption Angstrom Exponent in AERONET and related data as an indicator of aerosol composition. *Atmos. Chem. Phys. Discuss.* **2010**, *10*, 1155–1169. [[CrossRef](#)]

55. Stein, A.F.; Draxler, R.R.; Rolph, G.D.; Stunder, B.J.B.; Cohen, M.D.; Ngan, F. NOAA's HYSPLIT Atmospheric Transport and Dispersion Modeling System. *Bull. Am. Meteorol. Soc.* **2015**, *96*, 2059–2077. [[CrossRef](#)]
56. Lu, H.; Yi, S.; Xu, Z.; Zhou, Y.; Zeng, L.; Zhu, F.; Feng, H.; Dong, L.; Zhuo, H.; Yu, K.; et al. Chinese deserts and sand fields in Last Glacial Maximum and Holocene Optimum. *Chin. Sci. Bull.* **2013**, *58*, 2775–2783. [[CrossRef](#)]
57. Xie, Y.; Zhang, Y.; He, K.; Zhou, J.; Kang, C. Features of sand-dust deposits in Harbin city, China. *Chin. Geogr. Sci.* **2006**, *16*, 327–333. [[CrossRef](#)]
58. Sugimoto, N.; Shimizu, A.; Nishizawa, T.; Matsui, I.; Jin, Y.; Khatri, P.; Irie, H.; Takamura, T.; Aoki, K.; Thana, B. Aerosol characteristics in Phimai, Thailand determined by continuous observation with a polarization sensitive Mie–Raman lidar and a sky radiometer. *Environ. Res. Lett.* **2015**, *10*, 065003. [[CrossRef](#)]
59. Campbell, J.R.; Reid, J.S.; Westphal, D.L.; Zhang, J.; Tackett, J.L.; Chew, B.N.; Welton, E.J.; Shimizu, A.; Sugimoto, N.; Aoki, K.; et al. Characterizing the vertical profile of aerosol particle extinction and linear depolarization over Southeast Asia and the Maritime Continent: The 2007–2009 view from CALIOP. *Atmos. Res.* **2013**, *122*, 520–543. [[CrossRef](#)]
60. Fu, T.-M.; Jacob, D.J.; Wittrock, F.; Burrows, J.P.; Vrekoussis, M.; Henze, D.K. Global budgets of atmospheric glyoxal and methylglyoxal, and implications for formation of secondary organic aerosols. *J. Geophys. Res. Space Phys.* **2008**, *113*, 15. [[CrossRef](#)]
61. Alvarado, L.; Richter, A.; Vrekoussis, M.; Wittrock, F.; Hilboll, A.; Schreier, S.; Burrows, J. An improved glyoxal retrieval from OMI measurements. *Atmos. Meas. Tech.* **2014**, *7*, 4133. [[CrossRef](#)]
62. Vakkari, V.; Kerminen, V.-M.; Beukes, J.P.; Tiitta, P.; Van Zyl, P.G.; Josipovic, M.; Venter, A.D.; Jaars, K.; Worsnop, D.R.; Kulmala, M.; et al. Rapid changes in biomass burning aerosols by atmospheric oxidation. *Geophys. Res. Lett.* **2014**, *41*, 2644–2651. [[CrossRef](#)]
63. Khatri, P.; Takamura, T.; Nakajima, T.; Estellés, V.; Irie, H.; Kuze, H.; Campanelli, M.; Sinyuk, A.; Lee, S.-M.; Sohn, B.J.; et al. Factors for inconsistent aerosol single scattering albedo between SKYNET and AERONET. *J. Geophys. Res. Atmos.* **2016**, *121*, 1859–1877. [[CrossRef](#)]



© 2020 by the authors. Licensee MDPI, Basel, Switzerland. This article is an open access article distributed under the terms and conditions of the Creative Commons Attribution (CC BY) license (<http://creativecommons.org/licenses/by/4.0/>).